ELSEVIER

A least-squares finite element formulation for unsteady incompressible flows with improved velocity–pressure coupling

J.P. Pontaza *

Department of Mechanical Engineering, Texas A&M University, College Station, TX 77843-3123, USA

Abstract

In the weak form Galerkin formulation for incompressible flows, the pressure has a well-understood role. At all times, it may be interpreted as a Lagrange multiplier that enforces the divergence-free constraint on the velocity field. This is not the case in least-squares formulations for incompressible flows, where the divergence-free constraint is enforced in a least-squares sense in a variational setting of residual minimization. Thus, the role of the pressure in a least-squares formulation is rather vague. We find that this lack of velocity–pressure coupling in least-squares formulations may induce spurious temporal pressure oscillations when using the non-stationary form of the equations. We present a least-squares formulation with improved velocity–pressure coupling, based on the use of a regularized divergence-free constraint. A first-order system least-squares (FOSLS) approach based on velocity, pressure and vorticity is used to allow the use of practical C^0 element expansions in the finite element model. We use high-order spectral element expansions in space and second- and third-order time stepping schemes. Excellent conservation of mass and accuracy of computed pressure metrics are demonstrated in the numerical results.
© 2006 Elsevier Inc. All rights reserved.

Keywords: Least-squares; Incompressible flow; Spectral/*hp* methods

1. Introduction

1.1. Background

Finite element models based on least-squares variational principles are attractive alternatives to the weak form Galerkin models and their stabilized versions, and are the focus of this work. Finite element formulations based on least-squares principles give rise to unconstrained minimization problems through a variational framework of *residual* minimization. The idea is to define the least-squares functional as the sum of the squares of the governing equations residuals measured in suitable norms of Hilbert spaces. Provided the (linearized)

---

governing equations (augmented with suitable boundary and initial conditions) have a unique solution, the least-squares functional will have a unique minimizer. Moreover, if the induced energy norm is equivalent to a norm of a suitable Hilbert space, optimal properties of the resulting least-squares formulation can be established.

The numerical solution of the incompressible Navier–Stokes equations using least-squares based finite element models is among the most popular applications of least-squares methods [14]. Least-squares formulations for incompressible flows circumvent the inf–sup condition, thus allowing equal-order interpolation of velocities and pressure, and result (after suitable linearization) in linear algebraic systems with a symmetric positive definite (SPD) coefficient matrix. This translates into easy algorithm development and enables the use of robust and fast iterative solvers for SPD systems, such as matrix-free preconditioned conjugate gradient (PCG) algorithms.

The drawback of least-squares formulations is that these have associated with them the requirement of *higher regularity* of the finite element spaces. The degree of necessary smoothness is dictated by the differentiability requirements of the governing equation(s) under consideration and/or the norms used to measure their residuals in the least-squares functional.

To reduce the higher regularity requirements and allow the use of practical C^0 element expansions in the least-squares finite element model, the governing equation(s) are first transformed into an equivalent first-order system and the least-squares functional defined by measuring their residuals in terms of L_2 norms only. This approach renders the formulation *practical*, in the sense that existing computational frameworks based on C^0 expansions are easily adapted to the least-squares formulations. Transformation of the governing equations to an equivalent first-order system may necessarily imply that additional independent variables need be introduced, implying an increase in cost. However, the auxiliary variables may be argued to be beneficial as they may represent physically meaningful variables, e.g., vorticity, and will be directly approximated in the model.

In the context of *stationary* incompressible flows, least-squares formulations have been documented of lacking in the enforcement of the divergence-free constraint (i.e., poor conservation of mass) [2,3,7]. In our work we advance the use of high-order element expansions (*p*-levels $\geqslant 4$) [19], which mitigate poor conservation of mass and achieve exponentially fast decay of error measures for smooth solutions [19,21].

In the context of *non-stationary* (unsteady) incompressible flows, the pressure field displays an ill-behaved temporal evolution, when a perfectly smooth temporal evolution of the velocity field is obtained. We find that this ill-behaved response of the temporal evolution of the pressure field is particularly problematic for unsteady flows with inflow/outflow boundaries. Unsteady Dirichlet velocity flows (with prescribed-velocity everywhere; like lid-driven cavity flows) do not display this behavior. The sensitivity of least-squares formulations to boundary conditions is well known, and theoretical results for the stationary form of the equations in their vorticity first-order form exist [1,14].

Space–time decoupled formulations are especially sensitive to this problem, and some symptoms were reported in our work with the non-stationary form of the equations [20]. The use of high *p*-levels in time (when using a space–time coupled formulation) alleviates the symptoms but does not cure the problem. Further investigation into the matter revealed that a lack of velocity–pressure coupling in the least-squares formulation was at fault.

The lack of velocity–pressure coupling is evident in the least-squares formulation, as the pressure does not play a role in enforcing the divergence-free constraint. In the least-squares formulation, the velocity field will be solenoidal by virtue of minimizing the divergence-free constraint through the least-squares functional and not by virtue of the pressure field. Thus, the pressure does not have a well-defined role in the formulation.

We remark that this lack of velocity–pressure coupling seems to plague only least-squares simulations of unsteady flows, and is not present when dealing with the stationary form of the equations where there is no time evolution of the fields. Previous work on least-squares formulations for time-dependent problems of incompressible flows is scarce and has been presented by Tang and Tsang [25], Tang [24], Jiang [14], Pontaza [18] and Pontaza and Reddy [20]. However, the past work has failed to address the lack of velocity–pressure coupling. For instance, past work only reports time-evolution plots of the velocity field or velocity-related metrics (e.g., time history of vorticity at a point in space) and does not report plots of the time evolution of the pressure or pressure-related metrics (e.g., time history of the drag coefficient).

1.2. Present work

The objective of this paper is to present a least-squares formulation with improved velocity–pressure coupling. We use a regularized (perturbed) form of the divergence-free constraint to enforce the incompressibility condition:

$$\nabla \cdot \mathbf{u}_\varepsilon = -\varepsilon \, \delta p, \tag{1}$$

where ε is a small positive number, p is the pressure, and $\delta p = p^{(k)} - p^{(k-1)}$ for some positive index k, to be defined in Section 2. The exact divergence-free constraint is recovered as $\varepsilon \to 0$. In this limit, $\mathbf{u}_\varepsilon \to \mathbf{u}$, where $\mathbf{u}$ is divergence-free.

The regularized form of the divergence-free constraint (1) arises in penalty function methods [6,10,22], resulting from the approximation of the pressure as a Lagrange multiplier enforcing the divergence-free constraint. It also arises in artificial compressibility methods [4,9], with $\varepsilon = 1/(\beta \, \delta\tau)$, where β is the artificial compressibility parameter and $\delta\tau$ a pseudo-time step size.

Unlike classic penalty function methods, where (1) is used to eliminate the pressure from the momentum equations, we retain the pressure variable and minimize the residual of the regularized divergence-free constraint (1) directly; by including it in the least-squares functional. This practice prevents the parameter $1/\varepsilon$ from appearing in the discrete equations, thus avoiding ill-conditioning as $\varepsilon \to 0$.

The improved velocity–pressure coupling is due to recognizing the pressure as a Lagrange multiplier enforcing the divergence-free constraint and approximating its role by Eq. (1). For problems of the inflow/outflow type, our numerical results show that the use of the regularized divergence-free constraint (1) eliminates the ill-behaved temporal evolution of the pressure field. In addition, our numerical results indicate a lowering of the condition number and suppression of the dependence of the condition number on the time step size.

An overview of the paper is as follows. In Section 2, we present the regularized governing equations and the least-squares finite element formulation. In Section 3, we address some important issues regarding the implementation of the formulation. Section 4 is devoted to numerical examples showing the performance of the proposed formulation, in terms of conservation of mass and accuracy of pressure-related metrics. In Section 5 we present a summary and concluding remarks.

2. Regularized governing equations and least-squares formulation

Let $\overline{\Omega}$ be the closure of an open bounded region Ω in $\mathbb{R}^d$, where $d = 2$ or 3 represents the number of space dimensions, and $\mathbf{x} = (x_1, \ldots, x_d) = (x, y, z)$ be a point in $\overline{\Omega} = \Omega \cup \partial\Omega$, where $\partial\Omega = \Gamma$ is the boundary of Ω. We consider the solution of the regularized Navier–Stokes equations, which in dimensionless form can be stated as follows: Find the penalized velocity $\mathbf{u}_\varepsilon(\mathbf{x}, t)$ and pressure $p_\varepsilon(\mathbf{x}, t)$ such that

$$\frac{\partial \mathbf{u}_\varepsilon}{\partial t} + (\mathbf{u}_\varepsilon \cdot \nabla)\mathbf{u}_\varepsilon + \nabla p_\varepsilon - \frac{1}{Re}\nabla^2 \mathbf{u}_\varepsilon = \mathbf{f} \quad \text{in } \Omega \times (0, \tau], \tag{2}$$

$$\nabla \cdot \mathbf{u}_\varepsilon = -\varepsilon \, \delta p_\varepsilon \quad \text{in } \overline{\Omega} \times (0, \tau], \tag{3}$$

$$\mathbf{u}_\varepsilon(\mathbf{x}, 0) = {}^0\mathbf{u}(\mathbf{x}) \quad \text{in } \Omega, \tag{4}$$

$$\mathbf{u}_\varepsilon = \mathbf{u}^s(\mathbf{x}, t) \quad \text{on } \Gamma_u \times (0, \tau], \tag{5}$$

$$\hat{\mathbf{n}} \cdot \tilde{\boldsymbol{\sigma}}_\varepsilon = \mathbf{0} \quad \text{on } \Gamma_f \times (0, \tau], \tag{6}$$

where $\Gamma = \Gamma_u \cup \Gamma_f$ and $\Gamma_u \cap \Gamma_f = \emptyset$, τ is a real number (time) > 0, Re is the Reynolds number, $\tilde{\boldsymbol{\sigma}}_\varepsilon = -p_\varepsilon \mathbf{I} + (1/Re)\nabla \mathbf{u}_\varepsilon$, $\mathbf{f}$ is a dimensionless force, $\hat{\mathbf{n}}$ is the outward unit normal on the boundary of Ω, $\mathbf{u}^s$ is the prescribed velocity on the boundary Γ_u, the conditions on the boundary Γ_f in Eq. (6) are used to model outflow conditions [23], and in Eq. (4) the initial conditions are given. A well-posed problem requires $\nabla \cdot {}^0\mathbf{u} = 0$ in $\overline{\Omega}$. If $\Gamma = \Gamma_u$, the pressure may only be determined up to a constant in which case the average pressure is set to zero. In Eq. (3), $\delta p_\varepsilon = p_\varepsilon^{(k)} - p_\varepsilon^{(k-1)}$ for some positive index k, to be defined below.

It is easy to see that in the limit $\varepsilon \to 0$ the regularized equations approach the Navier–Stokes equations governing viscous incompressible flow. Better yet, it can be shown that solutions of the regularized equations approach solutions of the Navier–Stokes equations as follows [10]:

$$|\mathbf{u} - \mathbf{u}_\varepsilon^{(k)}|_1 + \|p - p_\varepsilon^{(k)}\|_0 = \mathcal{O}(\varepsilon^k),$$

where $0.0 < \varepsilon < 1.0$, $|\cdot|_1^2$ is a semi-norm associated with $H_0^1(\Omega)$ and $\|\cdot\|_0^2$ is the L_2 norm. The index k pertains to an iterative regularization of the divergence-free constraint or equivalently, an iterative penalization of the velocity field [6,10].

The iterative nature of the penalization is not necessary. Instead, the regularized divergence-free constraint $\nabla \cdot \mathbf{u}_\varepsilon = -\varepsilon p_\varepsilon$, with a non-iterative nature can be used. However, this particular form approaches solutions of the Navier–Stokes equations at a much slower rate [10]:

$$|\mathbf{u} - \mathbf{u}_\varepsilon|_1 + \|p - p_\varepsilon\|_0 = \mathcal{O}(\varepsilon).$$

In this work the iterative penalization is adopted and embedded with the Newton iterative procedure to linearize the governing equations.

Wishing to retain the ability to use practical C^0 expansions in the resulting finite element model, so that the formulation may be easily incorporated into existing computational frameworks, we reduce regularity requirements on the finite element spaces by introducing auxiliary variables to recast the governing equations as a set of first-order equations. Introducing the vorticity $\boldsymbol{\omega} = \nabla \times \mathbf{u}$ as an auxiliary variable, and dropping the ε subscript for convenience, we recast the governing equations as an equivalent first-order system and set out to minimize the first-order system least-squares (FOSLS) functional

$$\mathcal{I}(\mathbf{u}, p, \boldsymbol{\omega}; \mathbf{f}) = \frac{1}{2} \left(\left\| \frac{\partial \mathbf{u}}{\partial t} + (\mathbf{u} \cdot \nabla)\mathbf{u} + \nabla p + \frac{1}{Re} \nabla \times \boldsymbol{\omega} - \mathbf{f} \right\|_{0, \Omega \times (0, \tau]}^2 + \|\nabla \cdot \mathbf{u} + \varepsilon \delta p\|_{0, \Omega \times (0, \tau]}^2 \right.$$

$$\left. + \|\boldsymbol{\omega} - \nabla \times \mathbf{u}\|_{0, \Omega \times (0, \tau]}^2 + \|\nabla \cdot \boldsymbol{\omega}\|_{0, \Omega \times (0, \tau]}^2 + \|\hat{\mathbf{n}} \cdot (-p\mathbf{I} + (1/Re)\nabla \mathbf{u})\|_{0, \Gamma_f \times (0, \tau]}^2 \right), \tag{7}$$

where $\|\cdot\|_{0, \Omega \times (0, \tau]}^2$ denotes the L_2 norm of the enclosed quantity in space–time, we assumed that the chosen spaces for velocity satisfy the initial and boundary conditions, and requested that the outflow boundary condition be enforced in a weak sense through the least-squares functional.

Having defined the least-squares functional, the abstract least-squares minimization principle can be stated as

$$\text{find } U \in X \text{ such that } \mathcal{I}(U; \mathbf{f}) \leqslant \mathcal{I}(V; \mathbf{f}) \quad \forall V \in X, \tag{8}$$

where $U = (\mathbf{u}, p, \boldsymbol{\omega})$, $V = (\mathbf{v}, q, \boldsymbol{\chi})$, and X is a suitable vector space.

Prior to the minimization step, the residuals in the least-squares functional are linearized, e.g., using Newton's method. Upon minimization, one arrives at the following variational problem:

$$\text{find } U \in X \text{ such that } \mathcal{B}(U, V) = \mathcal{F}(V) \quad \forall V \in X, \tag{9}$$

where $\mathcal{B}$ is a linear symmetric form and $\mathcal{F}$ is a linear functional.

The finite element model is obtained by restricting (9) to the finite dimensional subspace X_{hp} of the infinite dimensional space X. This process leads to the discrete variational problem given by

$$\text{find } U^{hp} \in X_{hp} \text{ such that } \mathcal{B}(U^{hp}, V^{hp}) = \mathcal{F}(V^{hp}) \quad \forall V^{hp} \in X_{hp}. \tag{10}$$

We proceed to define a discrete problem by choosing appropriate finite element spaces for the velocity, pressure and vorticity. There are no restrictive compatibility conditions on the discrete spaces, so we choose the same finite element space for all primary variables. The discrete problem is solved in an iterative manner with respect to the regularization of the divergence-free constraint and Newton linearization.

The use of the regularized divergence-constraint improves the velocity–pressure coupling by adding terms like $(\varepsilon q, \nabla \cdot \mathbf{u})$ and $(\varepsilon p, \nabla \cdot \mathbf{v})$ to the symmetric form $\mathcal{B}$ of the least-squares projection, with $(\cdot, \cdot)$ denoting the L_2 inner product. It is no surprise that these L_2 inner products resemble that found in the weak form Galerkin

approach, $(q, \nabla \cdot \mathbf{u})$, where q (the virtual pressure) acts like a Lagrange multiplier enforcing the divergence-free constraint.

The overall success of the formulation lies in choosing an appropriate value for the parameter ε. If ε is set to zero or chosen too small, then the exact divergence-free constraint is recovered and the least-squares solution may be plagued with spurious temporal pressure oscillations, due to weak velocity–pressure coupling. If ε is chosen too large, the flow may no longer behave as incompressible due to an excessive relaxation of the divergence-free constraint.

The latter scenario poses no major problem as the incompressibility constraint may be still enforced properly by taking a sufficiently large number $(k = 1, 2, \ldots, K)$ of regularization steps. However, in practice we wish to take as few regularization steps as possible. In addition, in practice, for a given value of ε the velocity and pressure fields will cease to change after a fixed number of regularization steps. In other words, taking $K \to \infty$ will not recover the exact divergence-free constraint.

Based on experience with the numerical examples presented in Section 4, ε should be taken in the range 0.05–0.01. Interestingly, this is in agreement with typical values used and suggested for the artificial compressibility method [9], where $\varepsilon = 1/(\beta \, \delta \tau)$.

3. Implementation aspects

Before we present numerical results, we briefly discuss some important issues regarding the actual implementation of the formulation.

3.1. Time stepping

Note that in defining functional (7) we did not replace the temporal operator with a discrete equivalent. This results in a fully space–time coupled formulation, implied in the definition of functional (7) where the L_2 norm is defined in space–time. This implies, for example, that a two-dimensional time-dependent problem will be treated as a three-dimensional problem in space–time domain.

In a space–time decoupled formulation, discretization in space and time are done independently, and the temporal operator in the definition of functional (7) is replaced by a truncated Taylor series expansion in time domain. Each of the two approaches has its merits and drawbacks [20], but the space–time coupled formulation is obviously associated with increased computational cost.

To remain computationally fast, we adopt in this work space–time decoupled formulations only. For example, using the second-order trapezoidal rule time stepping scheme, we set out to minimize the following functional at each time step:

$$
\mathscr{I}_{\Delta t}(\mathbf{u}, p, \boldsymbol{\omega}; \mathbf{f}) = \frac{1}{2} \left(\left\| \left\{ \frac{2}{\Delta t}(\mathbf{u}^{s+1} - \mathbf{u}^s) - \dot{\mathbf{u}}^s \right\} + (\mathbf{u}^{s+1} \cdot \nabla)\mathbf{u}^{s+1} + \nabla p^{s+1} + \frac{1}{Re} \nabla \times \boldsymbol{\omega}^{s+1} - \mathbf{f}^{s+1} \right\|^2_{0,\Omega} \right.
$$
$$
\left. + \|\nabla \cdot \mathbf{u}^{s+1} + \varepsilon \, \delta p^{s+1}\|^2_{0,\Omega} + \|\boldsymbol{\omega}^{s+1} - \nabla \times \mathbf{u}^{s+1}\|^2_{0,\Omega} + \|\nabla \cdot \boldsymbol{\omega}^{s+1}\|^2_{0,\Omega} \right), \tag{11}
$$

where $\Delta t = t_{s+1} - t_s$ is the time increment, and it is implied that the problem will march in time. The trapezoidal rule time stepping scheme is non-self-starting, as the value of the acceleration at the previous time step, $\dot{\mathbf{u}}^s$, is not readily available at start-up. We perform the first few time steps using the first-order backward Euler scheme, and switch to the trapezoidal rule once the acceleration is available.

The trapezoidal rule is but a limiting case of a more general class of second-order time integrators. We use the generalized α-method (GAM) family of time integrators [5,8], which retain second-order accuracy in time and allow for user controlled high frequency damping by the single free integration parameter, $0.0 \leqslant \rho^h_\infty \leqslant 1.0$. For $\rho^h_\infty = 1.0$ the method is identical to the trapezoidal rule and for choices of $0 \leqslant \rho^h_\infty < 1.0$ high frequency damping is added with decreasing ρ^h_∞. We typically set $\rho^h_\infty < 1.0$ to damp out unresolved high frequencies that may excite the odd–even modes of the trapezoidal rule for long-term time integration.

Although in our experience the second-order time integrators perform well, we have also implemented a third-order time integrator. It is a stiffly stable third-order scheme, widely known as the third-order backward-differentiation scheme or BDF3 for short. The BDF3 time stepping scheme is also non-self-starting, so the first few time steps are taken using BDF1 and BDF2 schemes.

3.2. Scaling of the momentum equations residuals

The formulation and the resulting system of linear algebraic equations strongly depend on values of the parameters ε, $1/Re$ and Δt. As pointed out earlier, in the limit $\varepsilon \to 0$ we recover the exact divergence-free constraint. Since $1/\varepsilon$ does not appear in the formulation, there is no ill-behavior of the discrete equations associated with this limit.

The limit $1/Re \to 0$ corresponds to high Reynolds number flows, and is common in practice. Flow physics aside, this limiting value is well defined within the framework of the formulation.

Also of interest is the limit $\Delta t \to 0$. Computations using functional (11) indicate the deterioration of the numerical results in this limit. We find that by simply pre-multiplying the residual of the momentum equations by Δt alleviates this problem. For example, using the second-order trapezoidal rule time stepping scheme, we set out to minimize the following functional at each time step:

$$\mathscr{I}_{\Delta t}^{\star}(\mathbf{u}, p, \boldsymbol{\omega}; \mathbf{f}) = \frac{1}{2}\left(\left\|2(\mathbf{u}^{s+1} - \mathbf{u}^s) + \Delta t\left\{-\dot{\mathbf{u}}^s + (\mathbf{u}^{s+1} \cdot \nabla)\mathbf{u}^{s+1} + \nabla p^{s+1} + \frac{1}{Re}\nabla \times \boldsymbol{\omega}^{s+1} - \mathbf{f}^{s+1}\right\}\right\|_{0,\Omega}^2\right.$$

$$\left. + \|\nabla \cdot \mathbf{u}^{s+1} + \varepsilon \delta p^{s+1}\|_{0,\Omega}^2 + \|\boldsymbol{\omega}^{s+1} - \nabla \times \mathbf{u}^{s+1}\|_{0,\Omega}^2 + \|\nabla \cdot \boldsymbol{\omega}^{s+1}\|_{0,\Omega}^2\right) \tag{12}$$

Unless otherwise stated, computations presented in this paper are performed using the above scaling for the momentum equations residuals.

In the limit of interest, $\Delta t \to 0$, the recommended scaling yields deceptively low values for the momentum equations residuals when these are used as error indicators. Thus, we use functional $\mathscr{I}_{\Delta t}$, Eq. (11), to report the value of the least-squares functional.

In the present work, values as low as $\Delta t = 10^{-3}$ are used without deterioration of the numerical results. Previous work on least-squares formulations for unsteady incompressible flows consistently use $\Delta t \geqslant 0.10$, using values as high as $\Delta t = 0.50$ and $\Delta t = 1.0$ [14,24,25].

In the context of least-squares, we note that functional $\mathscr{I}_{\Delta t}^{\star}$, Eq. (12), can be interpreted as one where the momentum equation residual measure in functional $\mathscr{I}_{\Delta t}$, Eq. (11), has been pre-multiplied by a small constant – the time step size squared. This can be inevitably interpreted as a weighting of the residual measures, such that the other residual measures (e.g., the incompressibility constraint and the definition of vorticity) are given more weight to be better enforced. On the other hand, if one validly starts by using functional $\mathscr{I}_{\Delta t}^{\star}$, a similar argument could be posed regarding functional $\mathscr{I}_{\Delta t}$, which would give more weight to the momentum equation residual measure.

Nevertheless, the proposed formulation is not meant to rely on such ad hoc weighting schemes to improve conservation of mass or momentum. We show this by also demonstrating improved conservation of mass when using the non-scaled version of the least-squares functional, $\mathscr{I}_{\Delta t}$, in the numerical examples.

3.3. Numerical integration

The integrals in Eq. (10) are evaluated using Gauss quadrature rules. In our implementation the Gauss–Legendre rules are used and $p + 1$ quadrature points (in each coordinate direction) are used to evaluate the integrals, where p denotes the p-level of the spectral element basis.

Typically, in spectral element methods using Galerkin projections, Gauss–Lobatto–Legendre quadrature rules using $p + 1$ quadrature points (in each coordinate direction) are used to exploit discrete orthogonality properties which yield a diagonal mass matrix. In least-squares formulations the mass matrix has no special significance, and thus there is no definite advantage in using the Gauss–Lobatto–Legendre quadrature.

Although our computations indicate that there is little difference in the numerical results when using either quadrature rule, we prefer the Gauss–Legendre rule as a $p + 1$ quadrature rule is exact for polynomials of order $2p + 1$ whereas the Gauss–Lobatto–Legendre rule is exact for polynomials of order $2p - 1$.

3.4. Outflow boundary conditions

Artificial open boundaries are unavoidably introduced, for example, when addressing external flow problems where due to computational reasons one is forced to truncate the computational domain. The proper choice of boundary conditions at these open boundaries has long been a matter of controversy [23].

Weak form Galerkin formulations naturally give rise to open-type boundary conditions by virtue of the integration by parts step. These boundary conditions, given by Eq. (6), for the two-dimensional case are as follows:

$$\left(-p + \frac{1}{Re}\frac{\partial u}{\partial x}\right)n_x + \frac{1}{Re}\frac{\partial u}{\partial y}n_y = 0, \tag{13}$$

$$\frac{1}{Re}\frac{\partial v}{\partial x}n_x + \left(-p + \frac{1}{Re}\frac{\partial v}{\partial y}\right)n_y = 0, \tag{14}$$

where n_x and n_y are the x and y-components of the unit normal associated with the open-type boundary.

Least-squares formulations do not naturally give rise to such open-type boundary conditions; so we enforce them in a weak sense through the least-squares functional. This approach is not new and was first used in our previous work with least-squares formulations of incompressible flows [19,20].

For an outflow boundary whose unit normal is aligned with the x-axis, the outflow boundary conditions are

$$-p + \frac{1}{Re}\frac{\partial u}{\partial x} = 0, \quad \frac{1}{Re}\frac{\partial v}{\partial x} = 0. \tag{15}$$

The above expressions are also obtained when directly applying to the momentum equations the scalings used to approximate the spatial Orr–Sommerfeld equations [11,17].

Our numerical experiments indicate that outflow boundary conditions (15) perform well over a wide range of flow conditions. However, when the flow field in the close vicinity of the outflow boundary is in the highly non-linear regime (e.g., with high gradients) the condition $\partial v/\partial x = 0$ is problematic. Our observations are in accordance with those of Ol'shanskii and Staroverov [17].

Using the scaling argument used by Ol'shanskii and Staroverov [17], we arrive at the following outflow boundary conditions, which we find outperform boundary conditions (15) in the highly non-linear regime:

$$-p + \frac{1}{Re}\frac{\partial u}{\partial x} = 0, \quad \frac{\partial v}{\partial t} + u_\infty\frac{\partial v}{\partial x} = 0. \tag{16}$$

In (16), the condition $\partial v/\partial x = 0$ of (15) is replaced by a convective-type equation to be satisfied at the outflow boundary. The condition has an unsteady nature, which intuitively makes it more suitable for unsteady flows. These convective-type of outflow conditions are known to perform well and are mostly used in the finite difference community [23].

3.5. Nonlinear convergence

At each time step, we iteratively solve a linearized system of algebraic equations with respect to the Newton linearization. In turn, the system of linear algebraic equations may be solved using a direct (e.g., Cholesky factorization) or an iterative (e.g., preconditioned conjugate gradient) method.

Nonlinear convergence in velocities is declared when the criterion

$$\frac{\|\delta\mathbf{u}\|}{\|\mathbf{u}\|} = \frac{\|\mathbf{u}^{(k)} - \mathbf{u}^{(k-1)}\|}{\|\mathbf{u}^{(k)}\|} < 10^{-4}$$

is satisfied, where $\|\mathbf{u}^{(k)}\|$ denotes the discrete L_2 norm of the velocity vector at the kth nonlinear iteration on a given time step. Typically, three Newton iterations per time step are required to satisfy the above stopping criterion.

When using the regularized form of the divergence-free constraint, convergence of the pressure field is also monitored due to the iterative regularization, and is declared when $\|\delta p\|/\|p\| < 10^{-3}$. For the recommended range of values for ε (0.05–0.01), typically, three regularization steps per time step suffice to satisfy the criterion.

Since the regularization/Newton-linearization steps are embedded in each other, both criteria need to be satisfied to declare nonlinear convergence. Typically, a maximum of five regularization/Newton-linearization steps is allowed per time step. When using a small time step size, the criteria is satisfied in at most two or three steps. However, the number of steps till convergence is also largely dependent on the flow field and Reynolds number.

4. Numerical examples

4.1. Verification

In this first numerical example we wish to establish the second-order accuracy of the time integration scheme. To this end we consider a unit square $\overline{\Omega} = [0.0, 1.0] \times [0.0, 1.0]$ with Dirichlet velocity boundary data. We take the exact solution to the incompressible Navier–Stokes equations to be of the form:

$$
\begin{aligned}
u(x, y, t) &= \pi \sin^2(\pi x) \sin(2\pi y) \sin(t), \\
v(x, y, t) &= -\pi \sin^2(\pi y) \sin(2\pi x) \sin(t), \\
p(x, y, t) &= \cos(\pi x) \sin(\pi y) \sin(t).
\end{aligned}
\tag{17}
$$

The prescribed velocity field is, by construction, solenoidal and the source term $\mathbf{f}$ of the momentum equations is such that Eq. (17) is the exact solution.

The domain is spatially discretized using a 4×4 uniform quadrilateral finite element mesh. In each element we use 8th order nodal expansions (in each spatial direction), which is sufficient to represent the spatial variation of the analytic solution to within approximately 10^{-12} in the L_2 norm. Therefore any errors higher than this can be expected to be due to temporal accuracy. For the computations we set the Reynolds number to 100.

Computations are performed for $\varepsilon = 0.0$ and $\varepsilon = 0.01$, and both formulations yield the exact same results. This is explained by noting that this is a pure velocity Dirichlet problem, where no benefit is realized by using the regularized form of the divergence-free constraint.

The exact solution, given by Eq. (17), is used to prescribe Dirichlet velocity boundary conditions on the entire boundary and pressure is specified at a point. No boundary conditions for the vorticity are necessary. At each Newton linearization step the resulting linear algebraic system of equations with a SPD coefficient matrix is solved using banded Cholesky factorization.

The time evolution of the fields is computed for $t \in [0, 10]$ for decreasing time step sizes. The L_2 error in velocities, pressure and vorticity is recorded at $t = 5$ and plotted in Fig. 1 as a function of the time step size in a log–log scale. The errors decay at an algebraic rate with slope 2, as expected for the second-order accurate time marching scheme.

Estimates of the condition number of the global coefficient matrix computed using the standard LAPACK subroutine for banded SPD matrices, are shown in Fig. 2 as a function of time step size in a log–log scale. The condition number increases with decreasing time step size at an approximate rate of 1.43.

By construction, the analytic solution is independent of the Reynolds number. However, the discrete equations are dependent on the Reynolds number and it is instructive to see its effect on the accuracy of the computed solution and the condition number of the global coefficient matrix. Fig. 3 shows the L_2 error in velocities, pressure and vorticity for $\Delta t = 0.01$ at $t = 5$ and increasing Reynolds numbers. As the Reynolds number is increased the L_2 error increases up until $Re = 10^4$, at which point the change is negligible.

Fig. 4 shows the condition number for $\Delta t = 0.01$ and increasing Reynolds numbers. Similar to the behavior of the L_2 error, the condition number increases up until $Re = 10^3$, at which point the change is negligible.
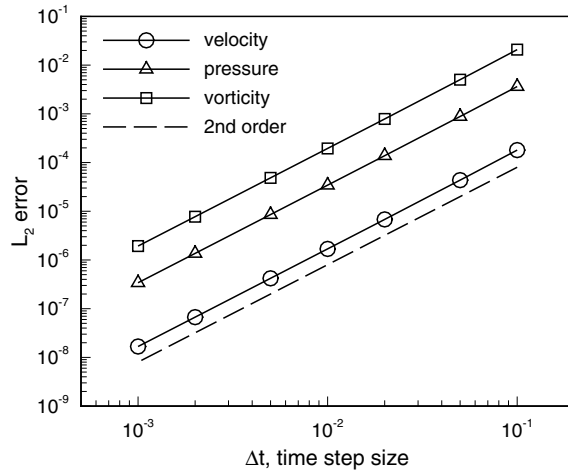
Fig. 1. Convergence of the velocity, pressure and vorticity fields at $t = 5$ in the L_2 norm for decreasing time step sizes. Verification of second-order accurate time stepping scheme.
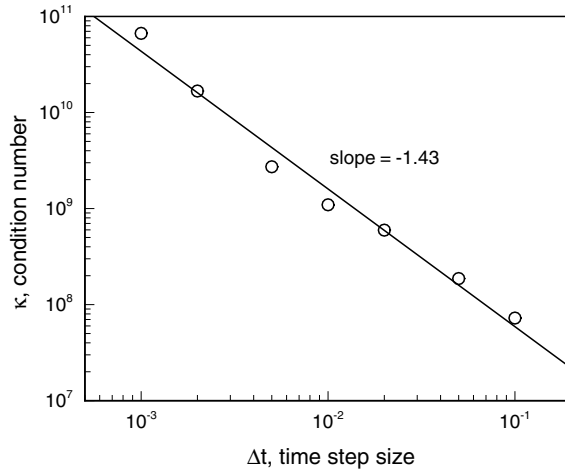

Fig. 2. Condition number of the least-squares Navier–Stokes global coefficient matrix for decreasing time step sizes.
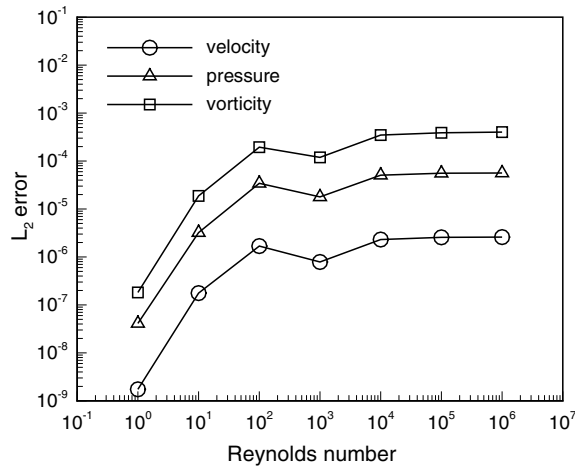

Fig. 3. L_2 error in velocity, pressure and vorticity fields for $\Delta t = 0.01$ at $t = 5$ for increasing Reynolds numbers.
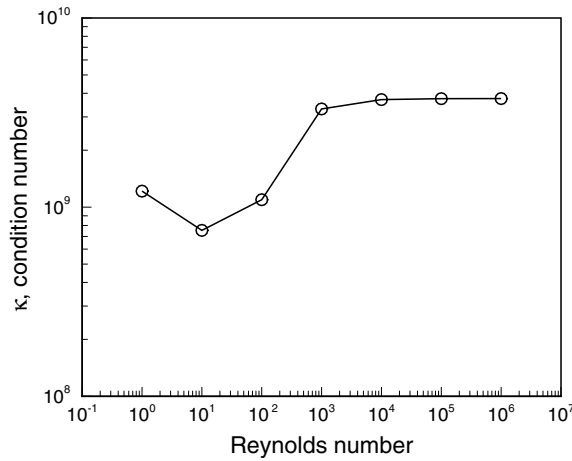
Fig. 4. Condition number of the least-squares Navier–Stokes global coefficient matrix for $\Delta t = 0.01$ and increasing Reynolds numbers.

Thus, the value of the condition number is much more sensitive to a change in the time step size than to a change in the Reynolds number.

4.2. Transient flow over a backward-facing step

4.2.1. Simplified step geometry

We consider the two-dimensional transient flow over a backward-facing step at $Re = 800$. This problem was presented in our earlier work with the non-stationary form of the Navier–Stokes equations [20]. Strong oscillations in time precluded a monotonic decay of the transients for space–time coupled and decoupled formulations. In some cases, when using the space–time decoupled approach, the transients were amplified leading to severe instabilities and the breakdown of the simulations. Here we repeat the simulation using the proposed formulation and show monotonic decay of the transients and excellent conservation of mass in time.

The geometry, mesh, boundary conditions, and initial conditions correspond exactly to those used in our previous work [20], and are briefly highlighted here for completeness. The simulations are performed using the simplified step geometry shown in Fig. 5, with the length of the channel extending a distance $L/H = 15$ downstream of the step. We discretize the domain, $\overline{\Omega} = [0, 15] \times [-0.5, 0.5]$, using 120 finite elements: four uniformly spaced elements along the height of the channel and 30 uniformly spaced elements along the length of the channel. The Reynolds number is based on the mean inlet velocity and the height of the channel.

The boundary conditions are: $u = v = 0$ on the horizontal walls and $u = u(y,t)$ and $v = 0$ on the inflow boundary and the step face. The outflow boundary conditions, given by Eq. (15), are imposed in a weak sense through the least-squares functional.

The initial condition is set to Poiseuille flow everywhere in the computational domain. The inlet condition is varied fast but smoothly from Poiseuille flow to flow over a backward-facing step, thus inducing a transient wave strong enough to excite sustained unsteady behavior, if that is the correct asymptotic steady-state behavior.
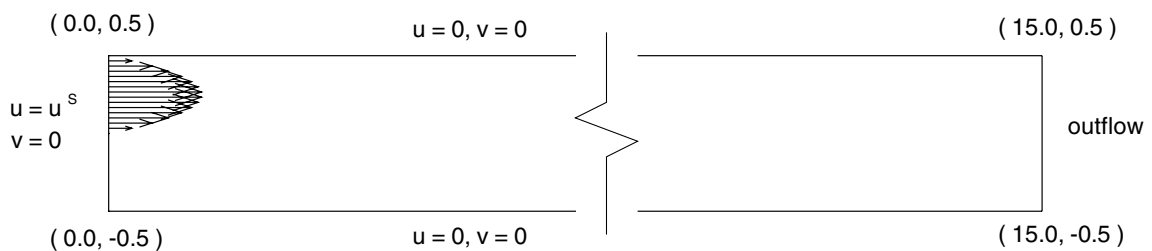

Fig. 5. Geometry and boundary conditions for flow over a backward-facing step: simplified step geometry.

At each regularization/Newton-linearization step, the linear system of equations with a SPD coefficient matrix is solved using a banded direct solver (Cholesky factorization). The banded direct solver is chosen, because the geometry naturally allows for a narrow band when the degrees of freedom are numbered across the channel height.

Time histories of the mass flow rates across three different stations along the channel are plotted in Fig. 6 for different values of ε, at a p-level of 6 and using $\Delta t = 0.10$. The expected response is $\dot{m}_x/\dot{m}_{in} = 1.0$ at all times. From Fig. 6 we see that excellent conservation of mass is achieved for all values of ε. Note that the scale on which the mass flow rates are plotted allows for a maximum deviation of $\pm 2.0\%$ mass loss/gain, which is never reached. From Fig. 6 we see that the deviation from $\dot{m}_x/\dot{m}_{in} = 1.0$ at all times is negligible.

Fig. 7 shows the time histories of the v-velocity component near the exit of the channel, at $(x,y) = (14,0)$. We see that for all cases we obtain a smooth and monotonic decay of the transient. The case $\varepsilon = 0.10$ displays some slight oscillations, presumably due to over-relaxation of the divergence-free constraint. Computations were also performed using lower spatial resolution (p-level 4) and higher spatial resolution (p-level 8). In both
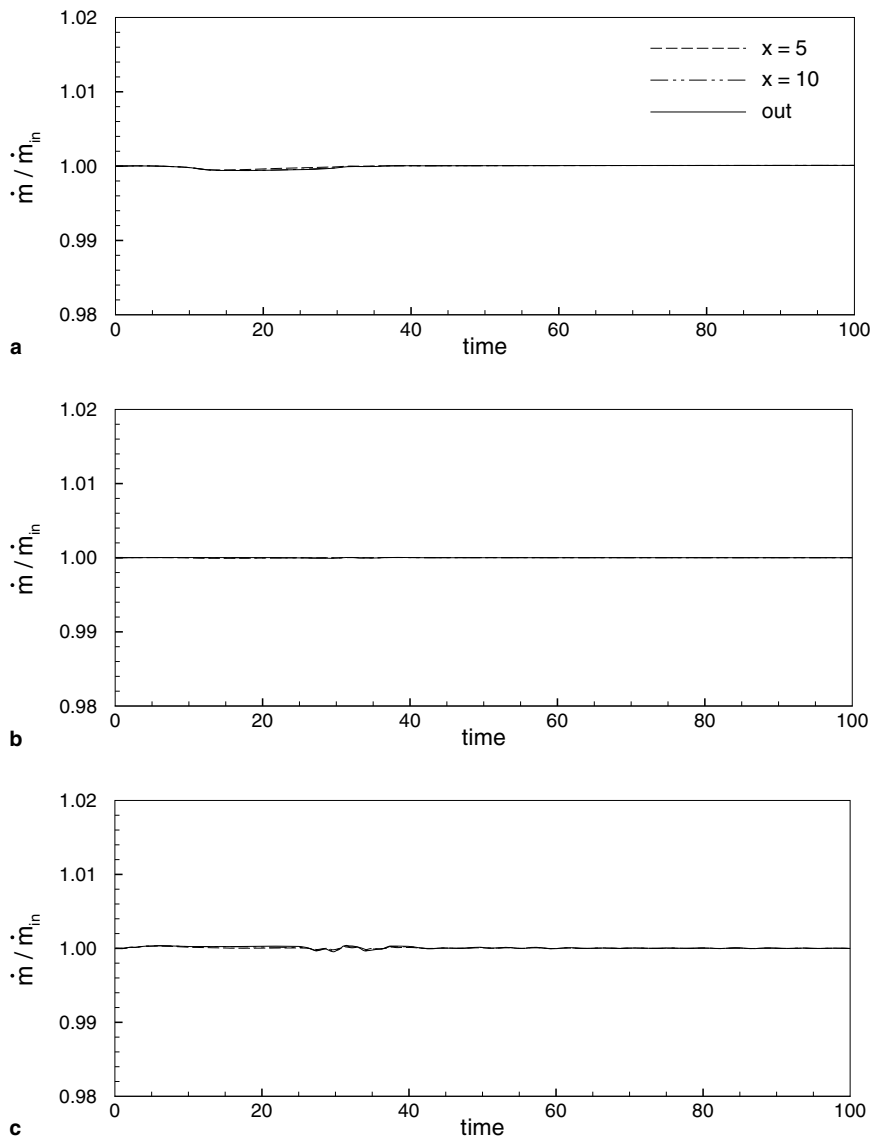
Fig. 6. Time histories of mass flow rates at $x = 5$, $x = 10$ and outlet for (a) $\varepsilon = 0.0$, (b) $\varepsilon = 0.01$ and (c) $\varepsilon = 0.10$. p-Level 6.
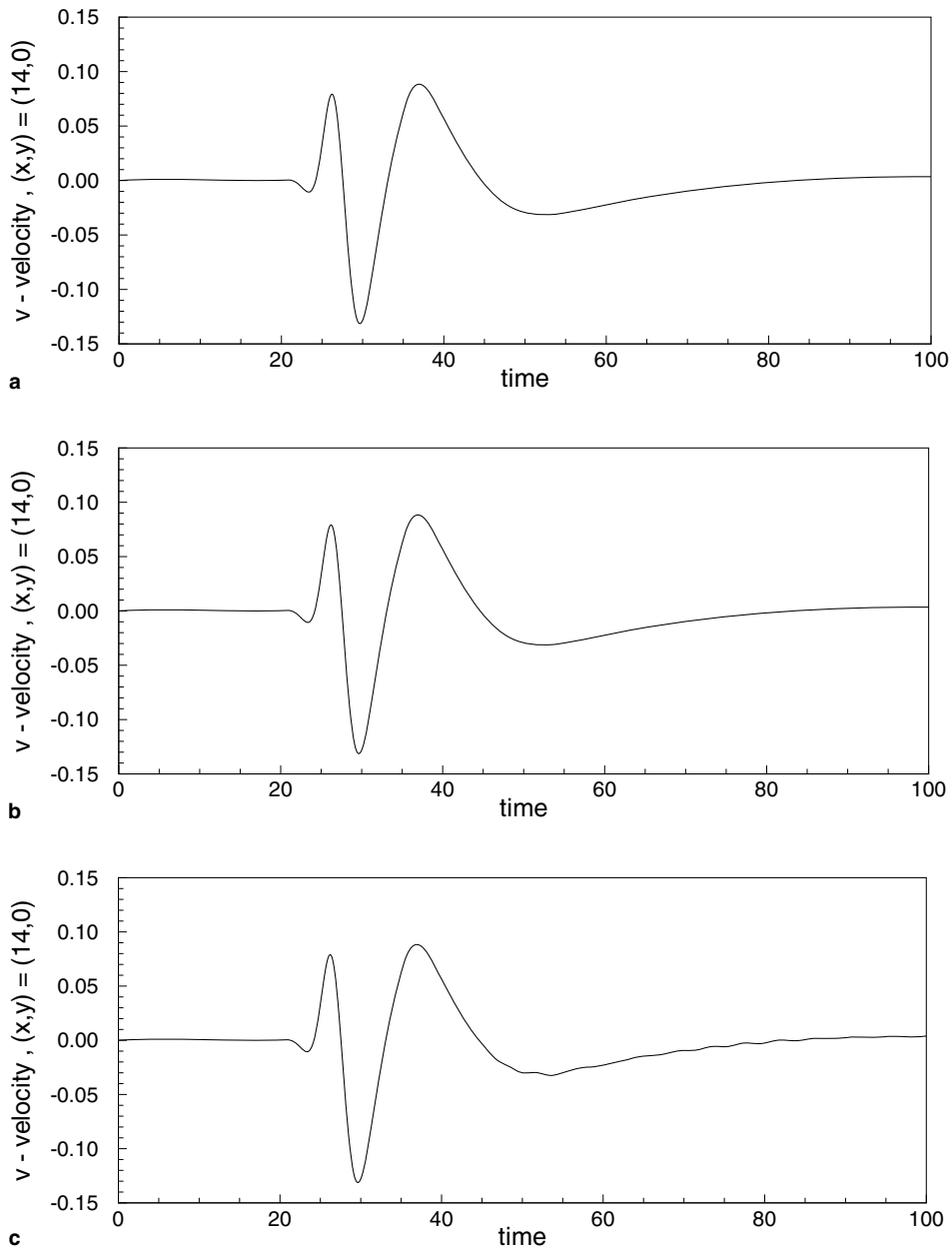
Fig. 7. Time histories of the v-velocity component near the exit of the channel: $(x,y) = (14,0)$ for (a) $\varepsilon = 0.0$, (b) $\varepsilon = 0.01$ and (c) $\varepsilon = 0.10$. p-Level 6.

of these cases, the response was as that observed for a p-level of 6: excellent conservation of mass and a mono-tonic decay of the transient.

In the steady-state, the primary recirculation zone has a reattachment point around $x = 6.0$ on the lower wall, while the secondary recirculation zone forms on the upper wall beginning near $x = 4.9$ with a reattach-ment point around $x = 10.4$. The steady-state recirculation lengths are in good agreement with those obtained using the stationary form of the equations [19].

Estimates of the condition number of the global coefficient matrix computed using the standard LAPACK subroutine for banded SPD matrices were recorded for computations using different p-levels and time step sizes, and are tabulated in Table 1 for $\varepsilon = 0.0$ and 0.01. The most salient feature is that for the case

Table 1
Condition number of the least-squares Navier–Stokes global coefficient matrix for increasing p-levels and decreasing time step size

ε	p-Level 4		p-Level 6		p-Level 8	
	$\Delta t = 0.10$	$\Delta t = 0.01$	$\Delta t = 0.10$	$\Delta t = 0.01$	$\Delta t = 0.10$	$\Delta t = 0.01$
0.00	2.0×10^9	1.7×10^{11}	1.6×10^{10}	1.0×10^{12}	6.5×10^{10}	3.4×10^{12}
0.01	4.1×10^7	4.1×10^7	3.3×10^8	3.8×10^8	1.6×10^9	3.3×10^9

$\varepsilon = 0.01$, $\Delta t = 0.10$ the condition number is lower by almost two orders of magnitude and hardly increases as the time step size is decreased.

Fig. 8 shows the condition number as a function of the time step size in a log–log scale for the cases $\varepsilon = 0.0$ and 0.01 at a p-level of 6. For the case $\varepsilon = 0.0$ the condition number increases as the time step is decreased at an approximate rate of 1.79, a slightly higher rate than that for the pure Dirichlet velocity problem considered earlier. In contrast, the case $\varepsilon = 0.01$ displays a lower condition number and negligible dependence on the time step size. We remark that this behavior is not unique to $\varepsilon = 0.01$, and the same behavior was observed for the case $\varepsilon = 0.10$. This behavior is remarkable and is to be exploited when using conjugate gradient algorithms to solve the system of equations with a SPD coefficient matrix, whose convergence rate depends strongly on the conditioning of the matrix.

Numerical results using the *non-scaled* least-squares functional (as discussed in Section 3.2) are shown in Figs. 9 and 10, where we plot the time histories of mass flow rates and v-velocity component for different values of ε, at a p-level of 6 and using $\Delta t = 0.10$. The case $\varepsilon = 0.0$ displays pronounced oscillatory behavior and total loss of conservation of mass, while the cases $\varepsilon = 0.01$ and 0.10 continue to give excellent conservation of mass and a monotonic decay of the transient. Thus, the cases $\varepsilon \neq 0.0$ give good conservation of mass by improved velocity–pressure coupling and not by virtue of the scaling. However, the case $\varepsilon = 0.0$ is clearly stabilized by virtue of the scaling.

4.2.2. Standard step geometry

We now consider the standard step geometry, where a portion of the channel upstream of the step of length $2H$ is included. The interest in this configuration is to determine whether the geometric singularity due to the sharp corner step will affect the predictive capabilities of the formulation. It is well known that high-order methods are very sensitive to geometric singularities and may have difficulty preserving monotonicity in their presence. In this context, high-order methods are not as robust as low-order methods. Moreover, the FOSLS adopted here introduced the vorticity as an auxiliary variable, which may grow unbounded near geometric singularities.
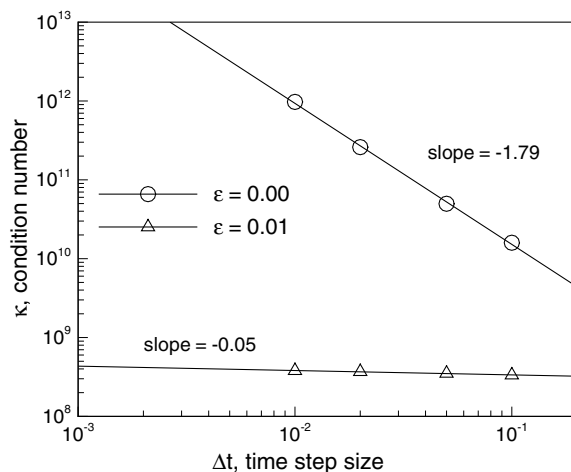

Fig. 8. Condition number of the least-squares Navier–Stokes global coefficient matrix for decreasing time step size at a p-level of 6. The case $\varepsilon = 0.01$ shows negligible dependence on the time step size.
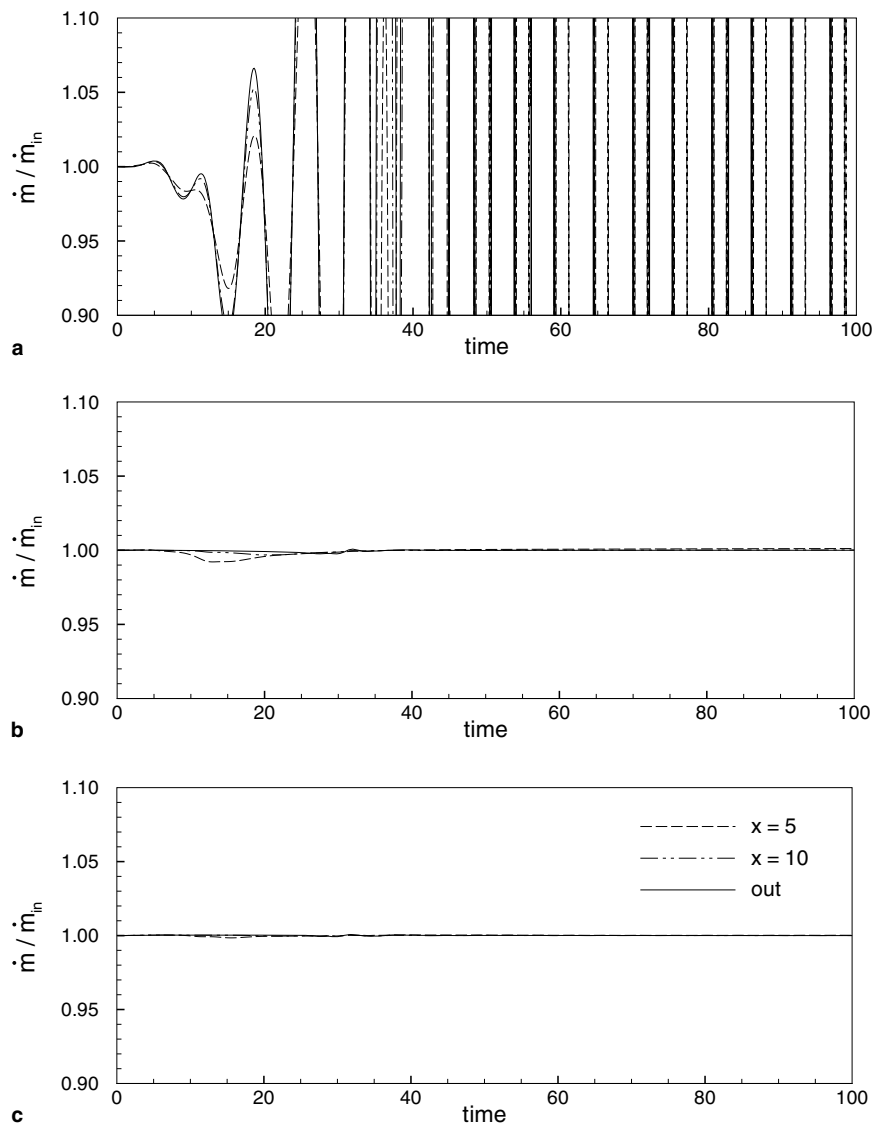
Fig. 9. Numerical results using non-scaled least-squares functional. Time histories of mass flow rates at $x = 5$, $x = 10$ and outlet for (a) $\varepsilon = 0.0$, (b) $\varepsilon = 0.01$ and (c) $\varepsilon = 0.10$. p-Level 6.

We prescribe a "non-smooth" initial condition, consisting of zero-initial fields and the fast release of incompressible fluid at the entrance of the channel at $t = 0$. The fluid is discharged fast, reaching its peak inlet velocity according to a hyperbolic function in time.

Simulations were carried out using the regularized form of the divergence-free constraint with $\varepsilon = 0.01$ at p-levels of 4, 6 and 8, using the mesh shown in Fig. 11, where a close-up view of the discretization around the corner step is shown. All the simulations gave a monotonic decay of the transient and excellent conservation of mass in time.

Time histories of the mass flow rates across three different stations along the channel for $t \in [0, 25]$ are plotted in Fig. 12 for the simulation at a p-level of 8. Initially, due to the "non-smooth" initial condition, there are slight oscillations in the time history of the mass flow rates. Fig. 13 shows the time history of the v-velocity component 1 unit downstream of the channel's outlet for $t \in [0, 200]$. A monotonic decay of the sharp transient is observed.
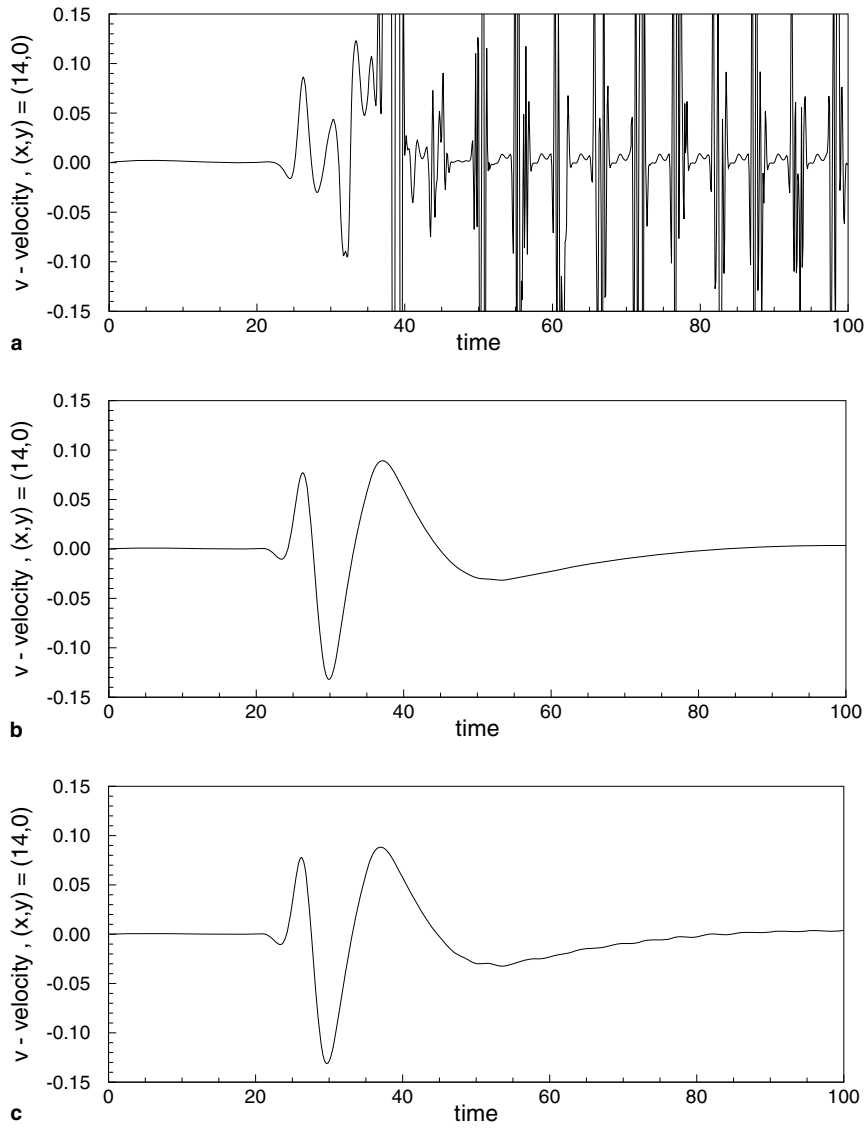
Fig. 10. Numerical results using non-scaled least-squares functional. Time histories of the v-velocity component near the exit of the channel: $(x, y) = (14, 0)$ for (a) $\varepsilon = 0.0$, (b) $\varepsilon = 0.01$ and (c) $\varepsilon = 0.10$. p-Level 6.
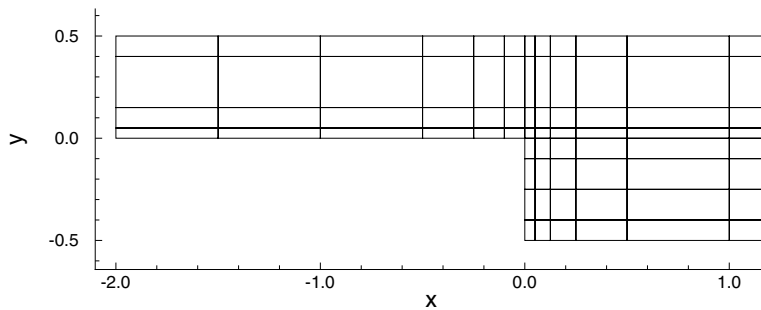

Fig. 11. Flow over a backward-facing step: standard step geometry. Close-up view of the discretization around the corner step.
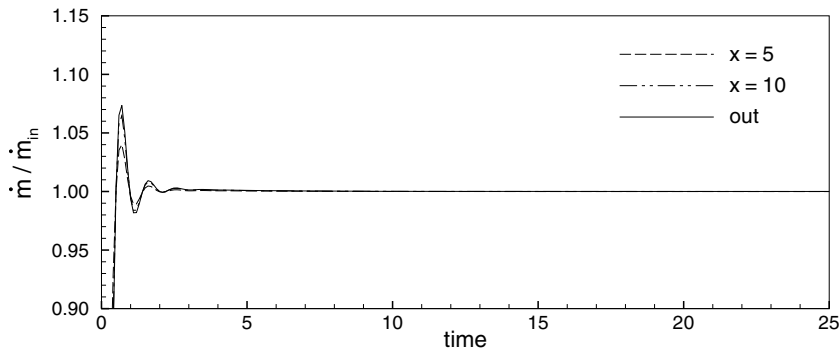
Fig. 12. Time histories of mass flow rates at $x = 5$, $x = 10$ and outlet for $\varepsilon = 0.01$. Standard step geometry, zero-initial fields. p-Level 8.
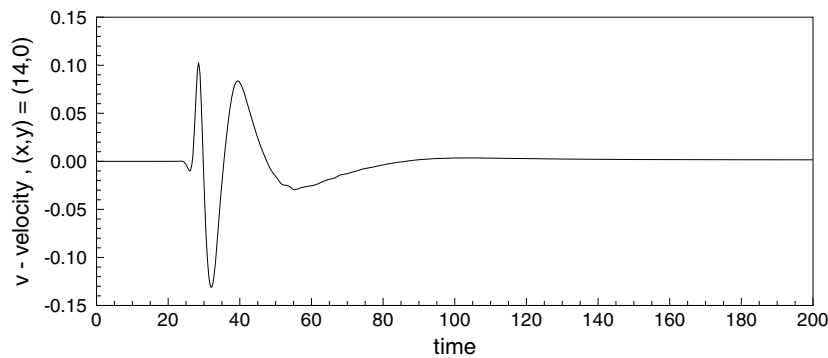
Fig. 13. Time history of the v-velocity component near the exit of the channel for $\varepsilon = 0.01$. Standard step geometry, zero-initial fields. p-Level 8.

Fig. 14 shows the time history of pressure contours during pronounced transients in the channel, $t \in [0, 50]$. The transient wave travels through the entire channel length. The main flow coming from the inlet follows a sinuous path through the channel, forming a series of eddies along the upper and lower wall. The pressure gradients caused by these eddies can be seen in these snapshots of the pressure field. Eventually the weaker eddies along the channel length die out and the flow reaches a steady state with the expected two major recirculation zones. From the numerical results we conclude that the sharp corner step did not hinder the capabilities of the formulation.

4.3. Circular cylinder moving in a narrow channel

This is the model problem to test conservation of mass due to Chang and Nelson [3], where a cylinder of unit diameter, D, is moving in a narrow channel of height $1.5D$. The finite element mesh in the geometry prescribed by Chang and Nelson [3] consists of 88 finite elements and is shown in Fig. 15.

The boundary conditions are $u = 1$, $v = 0$ at the upstream and lateral boundaries and no-slip boundary conditions, $u = v = 0$, at the cylinder surface. The outflow boundary conditions, given by Eq. (15), are imposed in a weak sense through the least-squares functional.

Here we wish to simulate an unsteady Navier–Stokes flow at $Re = 100$. To this end, the upper channel wall is shifted up by 0.03 units to promote the desired unsteadiness and the outflow boundary is moved downstream by 5.0 units to allow the wake to become well developed. Mass flow rates are computed at the crown of the cylinder, where the gap between the channel walls and cylinder surface is the smallest, and at the outflow of the channel.

At each regularization/Newton-linearization step, the linear system of equations with a SPD coefficient matrix is solved using a matrix-free conjugate gradient algorithm with a Jacobi preconditioner. PCG conver-
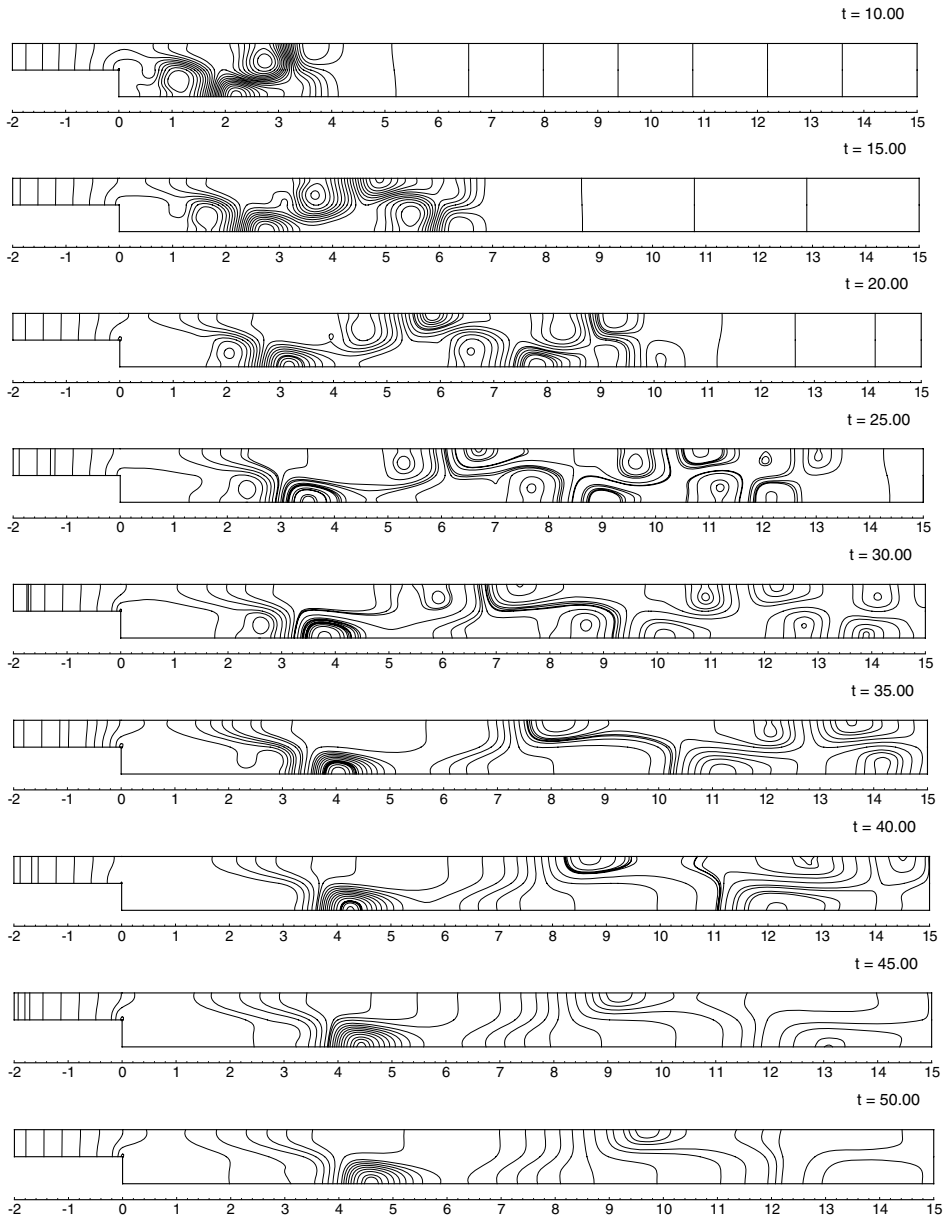
Fig. 14. Time history of pressure contours during pronounced transients in the channel, $t \in [0, 50]$. Standard step geometry, zero-initial fields, $\varepsilon = 0.01$. p-Level 8.

gence was declared when the norm of the residual associated with the linear algebraic system of equations was less than 10^{-6}.

Unlike the previous numerical example, where the flow field evolved towards a steady state, this problem sustains a periodic unsteady flow field. Vortex shedding occurs at a well-defined frequency of $St = 1/1.88 = 0.5319$. To adequately resolve the temporal evolution of the flow field we set $\Delta t = 0.02$, which gives a temporal resolution allowing for slightly over 90 time steps per shedding cycle. The third-order accurate BDF3 scheme is used for time stepping.

Time histories of the mass flow rates are plotted in Fig. 16 for $\varepsilon = 0.0$ and 0.01, at a p-level of 6. The response is plotted for $t \in [150, 200]$, by which time the flow field is well developed and has reached an
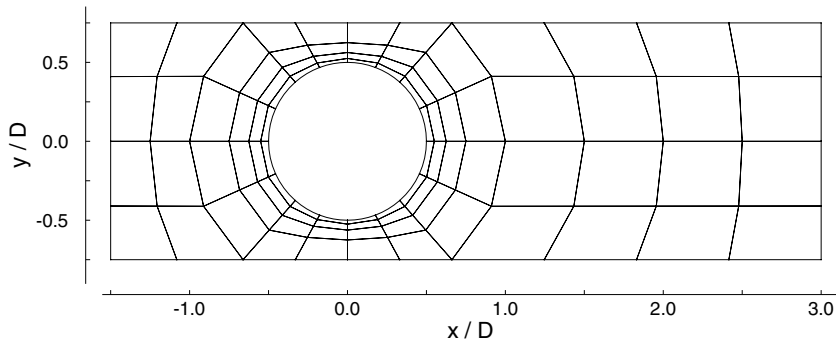
Fig. 15. Computational domain and mesh for the model problem to test conservation of mass due to Chang and Nelson [3].
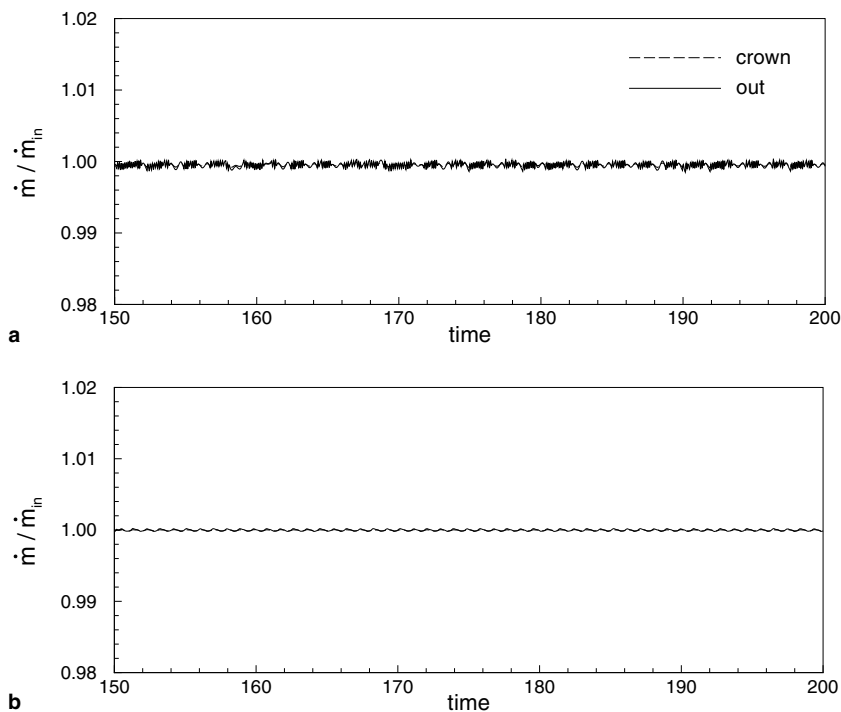

Fig. 16. Time histories of mass flow rates at the crown and outlet for (a) $\varepsilon = 0.0$ and (b) $\varepsilon = 0.01$. p-Level 6.

unsteady periodic behavior. The expected response is $\dot{m}_x/\dot{m}_{in} = 1.0$ at all times. Note that the scale on which the mass flow rates are plotted allows for a maximum deviation of $\pm 2.0\%$ mass loss/gain. Both formulations display excellent conservation of mass in time, showing negligible deviation from the expected response of $\dot{m}_x/\dot{m}_{in} = 1.0$ at all times. The case $\varepsilon = 0.0$ displays small-amplitude spurious oscillations that remain bounded and do not grow with time.

Fig. 17 shows the time history of the drag coefficient C_D and the base pressure coefficient C_{pb}. The case $\varepsilon = 0.0$ displays spurious temporal oscillations in these pressure metrics, while the case $\varepsilon = 0.01$ displays a smooth temporal evolution of the pressure metrics. A useful time-averaged drag and base pressure coefficient may still be extracted from the spurious temporal response, but with little confidence. A temporal response free of spurious oscillations is desirable and useful, as it may be used to characterize the shedding pattern and extract time-averaged metrics with confidence. Instantaneous pressure and vorticity contours in the channel are shown in Fig. 18.
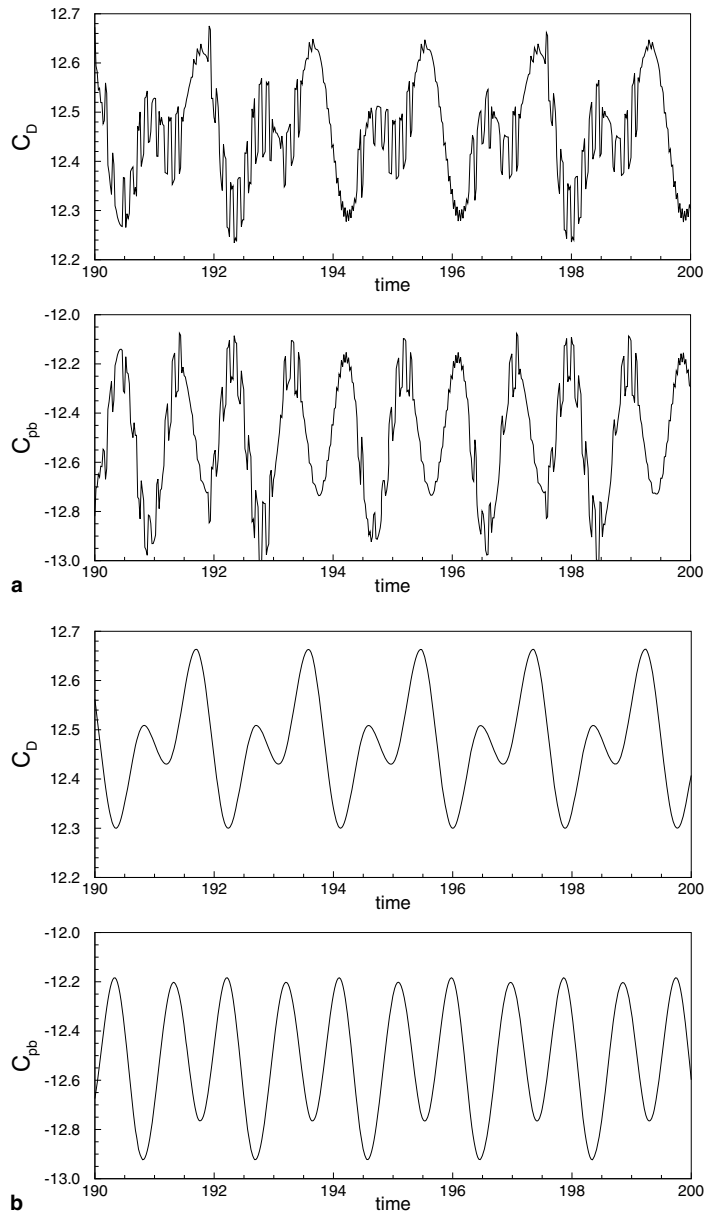
Fig. 17. Time history of the drag coefficient, C_D and base pressure coefficient, C_{pb}, for (a) $\varepsilon = 0.0$ and (b) $\varepsilon = 0.01$. p-Level 6.

Although an estimate of the condition number was not computed for this problem, one can infer that the case $\varepsilon = 0.01$ is better conditioned from the total PCG iteration count per time step (sum of PCG iterations taken during all the linearization steps on a given time step). The case $\varepsilon = 0.0$ required slightly over 3000 PCG iterations per time step, while the case $\varepsilon = 0.01$ required close to 1600 PCG iterations per time step; resulting in significant savings in terms of computational effort per time step.

Numerical results using the *non-scaled* least-squares functional (as discussed in Section 3.2) are shown in Fig. 19, showing time histories of mass flow rates for $\varepsilon = 0.0$ and 0.01, at a p-level of 6 and using $\Delta t = 0.10$. The case $\varepsilon = 0.0$ develops a pronounced oscillatory behavior resulting in total loss of conservation of mass and the simulation was manually stopped at $t = 60$. The case $\varepsilon = 0.01$ continues to give excellent conservation of mass. The stabilizing effect of the scaling for the case $\varepsilon = 0.0$ is evident from this and the previous numerical example.
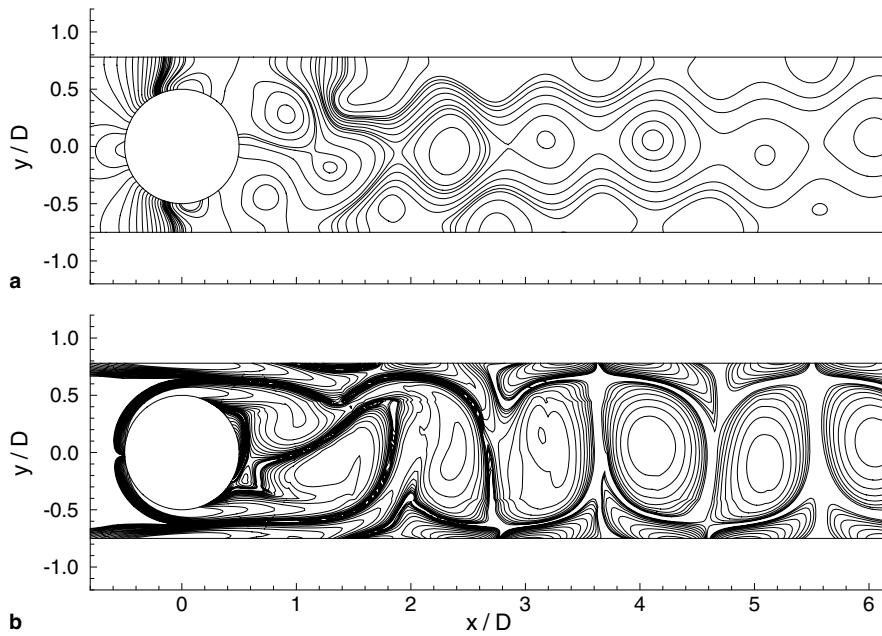
Fig. 18. Instantaneous (a) pressure and (b) vorticity contours in the channel for unsteady flow at $Re = 100$. $\varepsilon = 0.01$. p-Level 6.
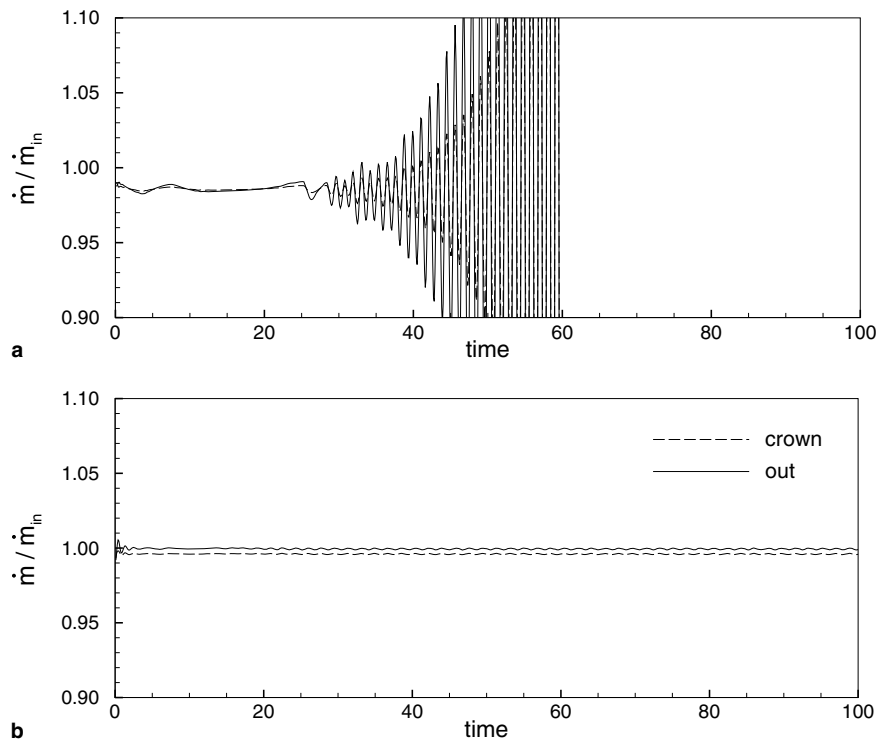

Fig. 19. Numerical results using non-scaled least-squares functional. Time histories of mass flow rates at the crown and outlet for (a) $\varepsilon = 0.0$ and (b) $\varepsilon = 0.01$. p-Level 6.

4.4. Unsteady flow past a circular cylinder

We consider the two-dimensional flow of an incompressible fluid past a circular cylinder. Having demonstrated excellent conservation of mass, smooth temporal evolution of the pressure field, and good matrix con-

ditioning for the proposed formulation, the focus of this last numerical example is to demonstrate the accuracy of computed pressure metrics and stability of the formulation with respect to moderately high Reynolds number flow conditions. For these computations we take $\varepsilon = 0.01$ and use the third-order accurate BDF3 scheme for time stepping.

The size of the computational domain is taken sufficiently large to preclude unwanted effects on computed flow metrics due to blockage, or location of inflow and outflow boundaries. The circular cylinder is of unit diameter, with its center at $(x, y) = (0, 0)$, and is placed in the rectangular region $\overline{\Omega} = [-14.5, 36.0] \times [-22.5, 22.5]$. The Reynolds number is based on the free-stream velocity and cylinder diameter.

At the upstream boundary of the computational domain both velocity components are assigned free-stream values: $u = u_\infty = 1$ and $v = v_\infty = 0$. At the lateral boundaries a no-flux boundary condition is imposed: $\partial u / \partial y = 0$ and $v = 0$, or equivalently $v = 0$, $\omega_z = 0$ (in view of $v = 0$). No-slip boundary conditions are specified at the cylinder surface: $u = v = 0$. Due to the strong vorticity sheets exiting the computational domain, we use the convective-type outflow boundary conditions given by Eq. (16), which are imposed in a weak sense through the least-squares functional.

The finite element mesh used for the computations is shown in Fig. 20, and consists of 834 finite elements. At each regularization/Newton-linearization step, the linear system of equations with a SPD coefficient matrix is solved using a matrix-free conjugate gradient algorithm with a Jacobi preconditioner. PCG convergence was declared when the norm of the residual associated with the linear algebraic system of equations was less than 10^{-6}.

To speed-up the turnaround time of the simulations, we use a parallelized version of our code. Blocks of contiguous elements with independent degree-of-freedom numbering are assigned to different processors and communication is only needed for data transfer at the block fringes, effectively minimizing the size of the transmission. Computations were performed in an IBM Regatta p690, using eight processors in parallel.

Simulations were performed for various Reynolds numbers in the range $Re \in [100, 10^3]$, at p-levels of 4 and 6 and using a time step size of $\Delta t = 0.05$. The chosen time step size allows for adequate temporal resolution, resulting in over 120 time steps per shedding cycle at $Re = 100$ and over 80 time steps per shedding cycle at $Re = 10^3$.

The simulations were also performed using a p-level of 8 and some limited runs using a p-level of 10 with $\Delta t = 0.02$, to demonstrate convergence of the following flow metrics: mean drag coefficient C_D, mean base pressure coefficient C_{pb}, Strouhal number St, and fluctuating lift coefficient C'_L. These results are recorded in Table 2 for selected Reynolds numbers.

At each Reynolds number, simulations were performed for $t \in [0, 100]$ to ensure a well-developed flow field. The simulations at higher Reynolds numbers were started using the lower Reynolds number solutions as an initial condition.
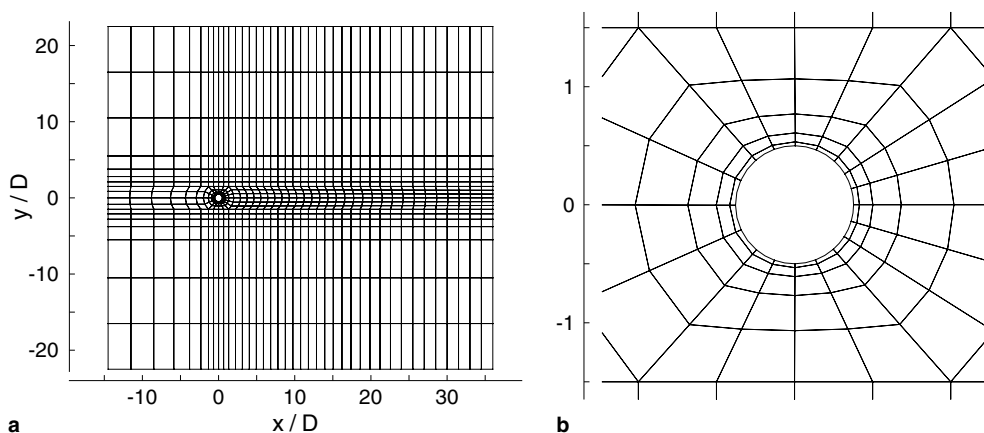

Fig. 20. Computational domain and mesh for flow past a circular cylinder. (a) Finite element mesh and (b) close-up view of the element distribution around the surface of the circular cylinder.

Table 2
Convergence of flow metrics with element expansion order for selected Reynolds numbers

Re	p-Level	Δt	C_D	$-C_{pb}$	St	C'_L
100	4	0.05	1.356	0.753	0.1667	0.335
	6	0.05	1.356	0.753	0.1667	0.334
	8	0.02	1.356	0.753	0.1667	0.334
300	4	0.05	1.378	1.200	0.2083	0.916
	6	0.05	1.391	1.219	0.2128	0.933
	8	0.02	1.390	1.218	0.2128	0.931
500	4	0.05	1.433	1.442	0.2273	1.148
	6	0.05	1.440	1.460	0.2273	1.182
	8	0.02	1.442	1.463	0.2273	1.182
800	4	0.05	1.500	1.656	0.2367	1.357
	6	0.02	1.488	1.653	0.2381	1.346
	8	0.02	1.493	1.666	0.2358	1.366
	10	0.02	1.494	1.667	0.2358	1.367
10^3	4	0.05	1.548	1.775	0.2381	1.476
	6	0.02	1.521	1.750	0.2404	1.439
	8	0.02	1.529	1.768	0.2392	1.462
	10	0.02	1.534	1.776	0.2392	1.471

Although the flow is three-dimensional in nature for $Re > 188$ [12], a two-dimensional simulation is still of interest in theoretical fluid mechanics. Flow metrics such as the mean drag and base pressure coefficients are over-predicted in two-dimensional simulations due to omission of spanwise wake effects with short correlation lengths.

Fig. 21 shows the computed time-averaged drag coefficients and Fig. 22 the computed time-averaged base pressure coefficients for increasing Reynolds numbers. The reference curve with which we compare our simulation results represents a smooth fit to the discrete set of two-dimensional simulation data points obtained by Henderson [12].

The results of Henderson [12] were obtained using a high-order time-splitting spectral element method [13,15]. In this approach, the Navier–Stokes system is represented by an advection problem and a sequence of elliptic Helmholtz-type problems, each of which are discretized using a weak-form Galerkin formulation.

Overall, our simulation results show good agreement with the reference curves over the range of Reynolds numbers considered, even when using a p-level of 4. In Fig. 22 we also plot the mean base pressure coefficient experimental measurements of Williamson and Roshko [26], showing that the flow becomes three-dimensional around $Re \approx 180$.

Fig. 23 shows computed instantaneous vorticity contours in the wake of the cylinder for increasing Reynolds number. The narrowing of the wake and the increase in shedding frequency, as the Reynolds number increases, is clear from these plots. We observe that at higher Reynolds numbers the vortices in the far-downstream wake coalesce and the region of coalescence moves upstream as the Reynolds number increases. In addition, the plots show evidence that the outflow boundary condition allows for a smooth exit of the flow field and does not distort the flow upstream.

To further test the stability of the formulation at higher Reynolds numbers, we increased the Reynolds number to $Re = 3900$. The simulation remained perfectly stable and predicted $C_D = 1.73$, $C_{pb} = -2.10$, and $St = 0.261$ for a p-level of 10 and $\Delta t = 1 \times 10^{-2}$. The predicted time-averaged base pressure coefficient and Strouhal number are in good agreement with the values reported by Ma et al. [16] for their high-order simulations at the same Reynolds number under conditions of two-dimensionality: $C_{pb} = -2.07$, $St = 0.268$.

One of the major obstacles we faced with respect to increasing Reynolds number was that the vorticity field in the near-wake of the cylinder needed to be well resolved to achieve suitable (e.g., three digit) convergence of the flow metrics. This is an unfortunate burden we need to deal with and stems from the adopted FOSLS
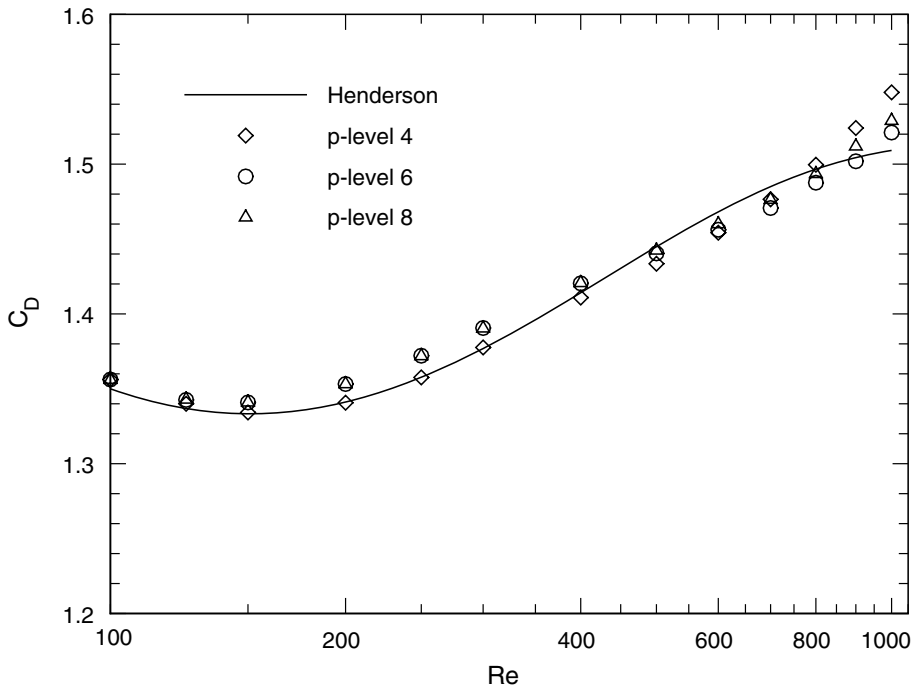
Fig. 21. Mean drag coefficient vs. Reynolds number for unsteady flow past a circular cylinder. Comparison of our 2-D simulation results with the 2-D simulation results of Henderson [12].
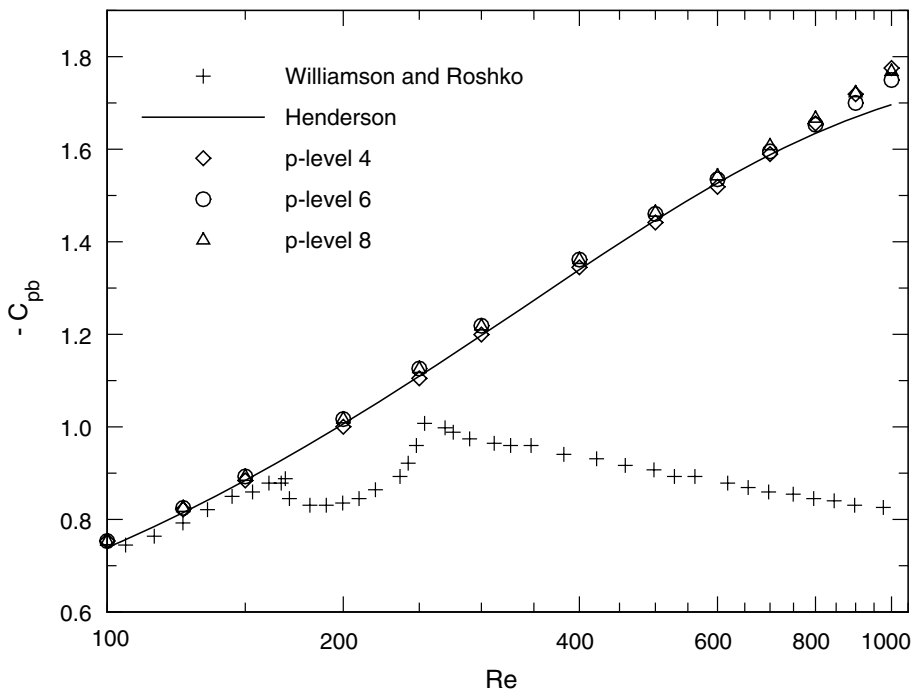

Fig. 22. Mean base pressure coefficient vs. Reynolds number for unsteady flow past a circular cylinder. Comparison of our 2-D simulation results with the 2-D simulation results of Henderson [12] and (3-D) experimental measurements of Williamson and Roshko [26].
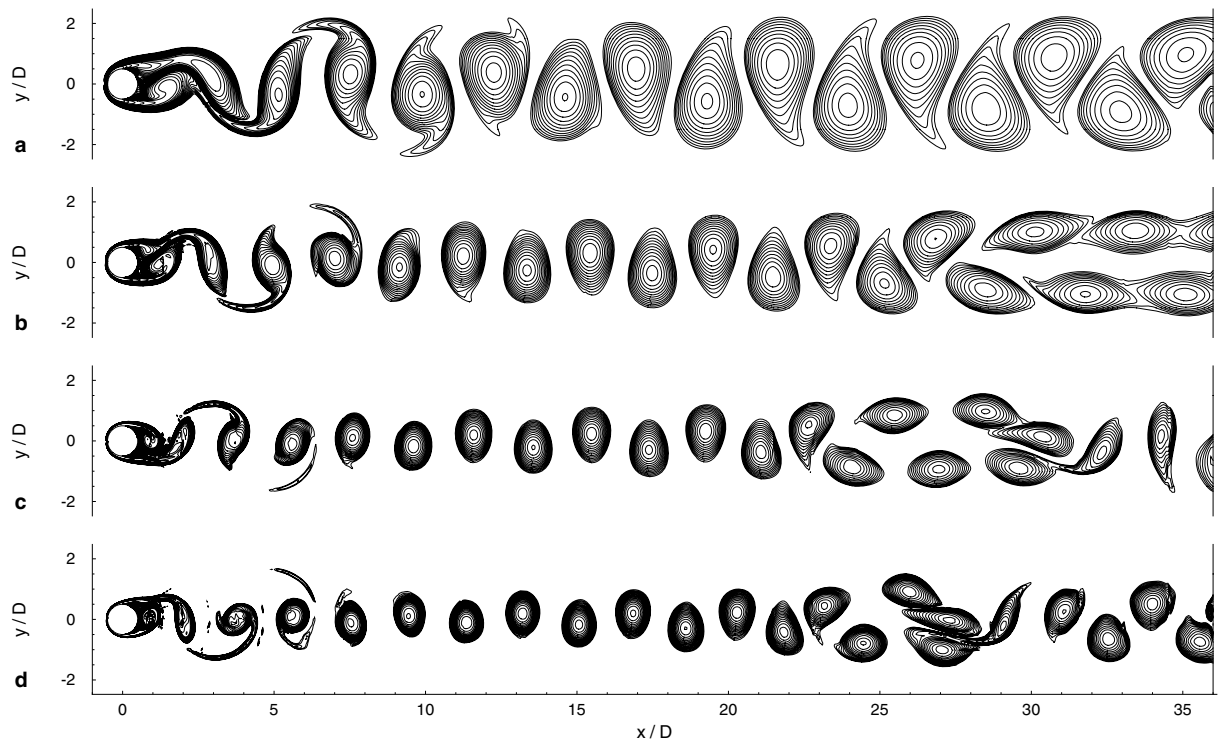
Fig. 23. Instantaneous vorticity contours for unsteady flow past a circular cylinder: (a) $Re = 150$, (b) $Re = 300$, (c) $Re = 500$ and (d) $Re = 10^3$.

$(\mathbf{u}, p, \omega)$ system which has vorticity as a primary variable. The vorticity field has much smaller scales and is more difficult to resolve. This explains the mesh grading we used in the wake of the cylinder.

In view of the near-wake mesh grading and the need to maintain geometric conformity, over 45% of the elements are wasted in the far-field where the solution is smooth. Here we would benefit from a non-conforming discretization, which would allow us to remove unnecessary elements from the far-field and place h- and/or p-type non-conforming elements in the near-wake of the cylinder. The least-squares functional naturally provides a sharp error-estimate that can be used to decide when to refine a particular element.

Although we did not implement a non-conforming discretization, we illustrate how the element-level values of the least-squares functional may be used to guide the mesh grading. Fig. 24 shows element-level values of the least-squares functional at an instant in time for flow conditions $Re = 200$, 500 and 10^3 at p-level 6. Elements that are colored white are those whose value of the least-squares functional is below 10^{-5}. These are elements in the far-field and small elements around the circular cylinder where the flow is well resolved. Elements that are colored black are those whose value of the least-squares functional is above 10^{-3}, and should be flagged for h- and/or p-refinement. We see that at higher Re the global value of the least-squares functional is dominated by those 15–30 elements in the near-wake that are colored black. We remark that in these elements the value of the least-squares functional is dominated by the momentum residuals, due to a lack of resolution on the vorticity field.

5. Summary and concluding remarks

We presented a least-squares finite element formulation for unsteady incompressible flows with improved velocity–pressure coupling. Numerical examples using a FOSLS finite element formulation with vorticity as an auxiliary variable were presented using high-order ($p \geqslant 4$) element expansions. Time stepping was performed by second- and third-order accurate schemes, using a proper scaling of the momentum equations to prevent deterioration of the numerical results as the time step size tends to zero.
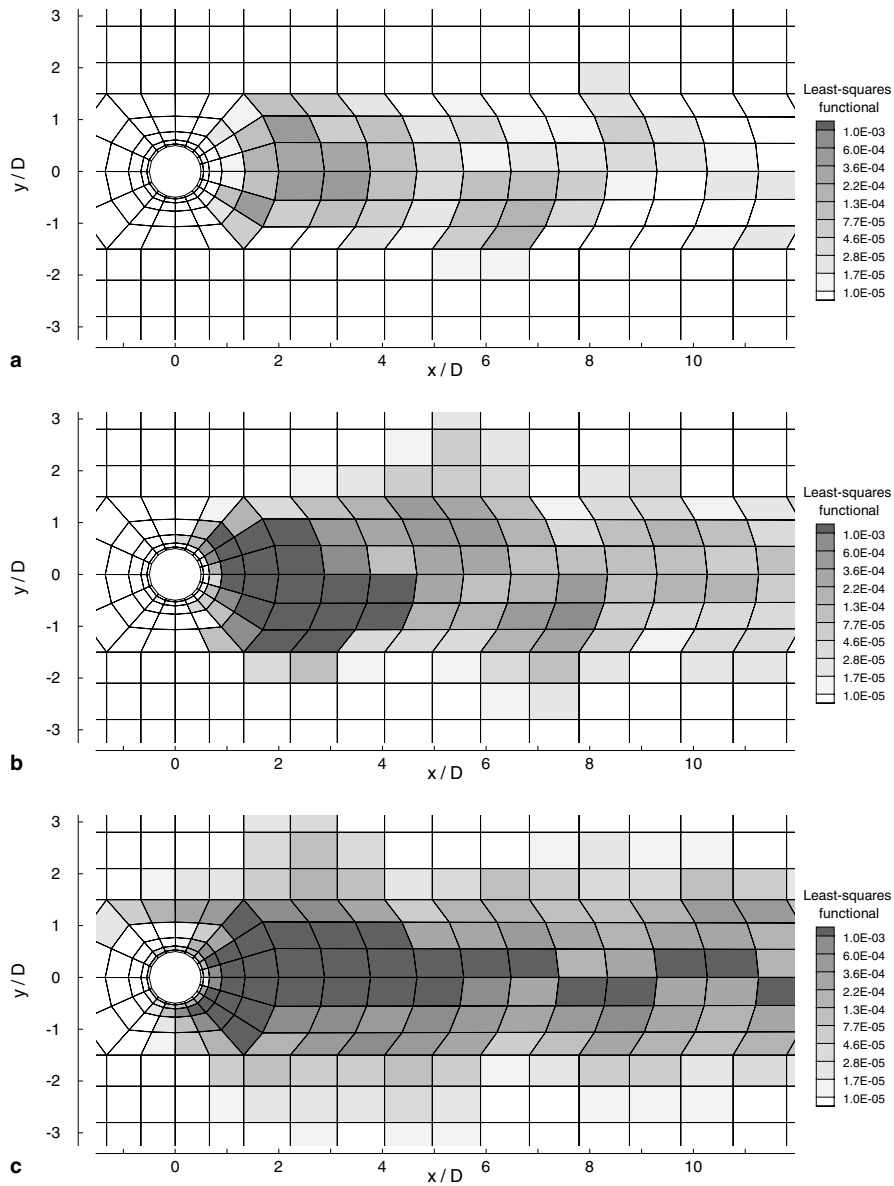
Fig. 24. Elements colored by instantaneous value of the least-squares functional for increasing Reynolds numbers: (a) $Re = 200$, (b) $Re = 500$ and (c) $Re = 10^3$. p-Level 6.

Acknowledgments

References

[1] P.B. Bochev, Analysis of least-squares finite element methods for the Navier–Stokes equations, SIAM J. Numer. Anal. 34 (1997) 1817–1844.
[2] P. Bolton, R.W. Thatcher, On mass conservation in least-squares methods, J. Comput. Phys. 203 (2005) 287–304.
[3] C.L. Chang, J.J. Nelson, Least-squares finite element method for the Stokes problem with zero residual of mass conservation, SIAM J. Numer. Anal. 34 (1997) 480–489.
[4] C. Chorin, A numerical method for solving incompressible viscous flow problems, J. Comput. Phys. 2 (1967) 12–26.
[5] J. Chung, G.M. Hulbert, A time integration algorithm for structural dynamics with improved numerical dissipation: The generalized α-method, J. Appl. Mech. 60 (1993) 371–375.
[6] C. Cuvelier, A. Segal, A.A. van Steenhowen, Finite Element Methods and Navier–Stokes Equations, D. Reidel Publishing Company, 1986.
[7] J.M. Deang, M.D. Gunzburger, Issues related to least-squares finite element methods for the Stokes equations, SIAM J. Sci. Comput. 20 (1998) 878–906.
[8] W. Dettmer, D. Peric, An analysis of the time integrator algorithms for the finite element solutions of incompressible Navier–Stokes equations based on a stabilised formulation, Comput. Meth. Appl. Mech. Eng. 192 (2003) 1177–1226.
[9] J.H. Ferziger, M. Peric, Computational Methods for Fluid Dynamics, Springer, 1997.
[10] M.D. Gunzburger, Finite Element Methods for Viscous Incompressible Flows, Academic Press, 1989.
[11] T. Hagstrom, Conditions at the downstream boundary for simulations of viscous incompressible flow, SIAM J. Sci. Statist. Comput. 12 (1991) 843–858.
[12] R.D. Henderson, Details on the drag curve near the onset of vortex shedding, Phys. Fluids 7 (1995) 2102–2105.
[13] R.D. Henderson, G.E. Karniadakis, Unstructured spectral element methods for simulation of turbulent flows, J. Comput. Phys. 122 (1995) 191–217.
[14] B.N. Jiang, The Least-Squares Finite Element Method, Springer-Verlag, New York, 1998.
[15] G.E. Karniadakis, M. Israeli, S.A. Orszag, High-order splitting methods for the incompressible Navier–Stokes equations, J. Comput. Phys. 97 (1991) 414–443.
[16] X. Ma, G.S. Karamanos, G.E. Karniadakis, Dynamics and low-dimensionality of a turbulent near wake, J. Fluid Mech. 410 (2000) 29–65.
[17] M.A. Ol'shanskii, V.M. Staroverov, On simulation of outflow boundary conditions in finite difference calculations for incompressible fluid, Int. J. Numer. Meth. Fluids 33 (2000) 499–534.
[18] J.P. Pontaza, Least-squares variational principles and the finite element method: theory, formulations, and models for solid and fluid mechanics, Ph.D. dissertation, Texas A&M University, 2003.
[19] J.P. Pontaza, J.N. Reddy, Spectral/*hp* least-squares finite element formulation for the Navier–Stokes equations, J. Comput. Phys. 190 (2003) 523–549.
[20] J.P. Pontaza, J.N. Reddy, Space–time coupled spectral/*hp* least-squares finite element formulation for the incompressible Navier–Stokes equations, J. Comput. Phys. 197 (2004) 418–459.
[21] M.M.J. Proot, M.I. Gerritsma, Least-squares spectral elements applied to the Stokes problem, J. Comput. Phys. 181 (2002) 454–477.
[22] J.N. Reddy, An Introduction to the Finite Element Method, second ed., McGraw-Hill, New Jersey, 1993.
[23] R.L. Sani, P.M. Gresho, Resume and remarks on the open boundary condition minisymposium, Int. J. Numer. Meth. Fluids 18 (1994) 983–1008.
[24] L.Q. Tang, A least-squares finite element method for time-dependent fluid flows and transport phenomena, Ph.D. dissertation, University of Kentucky, 1994.
[25] L.Q. Tang, T.T.H. Tsang, A least-squares finite element method for time dependent incompressible flows with thermal convection, Int. J. Numer. Meth. Fluids 17 (1993) 271–289.
[26] C.H.K. Williamson, A. Roshko, Measurements of base pressure in the wake of a cylinder at low Reynolds numbers, Zeit. Flugwissenschaf. Weltraumforsc. 14 (1990) 38–46.